

# Finite Element Method for the Two-Dimensional Poisson Equation: Theory and Numerical Simulation

Minseok Baek<sup>†</sup>

<sup>†</sup>Department of Mathematics, Inha University, Incheon, Republic of Korea

December 3, 2025

## Abstract

Many problems in science and engineering can be modeled as boundary value problems for the Poisson equation, and among numerical methods for solving such problems, the finite element method has become widely used because it can handle complicated domains and boundary conditions in a natural way. In this paper we consider the two-dimensional Poisson problem with homogeneous Dirichlet boundary conditions and formulate a Galerkin finite element method based on conforming piecewise linear elements on triangular meshes. Starting from the weak formulation, we introduce appropriate function spaces and finite element spaces, and derive a priori error estimates by combining Céa's lemma with standard interpolation error bounds. To validate the theory, we implement the finite element method in MATLAB and carry out numerical experiments on test problems with known exact solutions, using a sequence of successively refined meshes. On each mesh we compute the errors in the  $H^1$ - and  $L^2$ -norms and show that the observed convergence rates agree well with the theoretically predicted optimal orders. This confirms that the theoretical analysis of the finite element method for the two-dimensional Poisson equation is reflected accurately in actual computations, and provides a foundation for extending the framework to more general elliptic problems.

**Keywords:** Finite Element Method, Galerkin method, Poisson equation, a priori error estimate, convergence rate

**AMS Classification:** Primary 65N30; Secondary 35J05, 65N15.

## 1 Introduction

### 1.1 Background and Historical Overview of FEM

Many boundary value problems in science and engineering are modeled by partial differential equations (PDEs), for instance diffusion and heat conduction, electrostatics, linear elasticity, and incompressible flow. In realistic applications these PDEs are posed on geometrically complex domains with nontrivial boundary conditions, so that analytic solutions are rarely available and numerical approximation methods become essential.

Among classical numerical methods for PDEs, the finite element method (FEM) plays a central role. While finite difference and finite volume schemes are conceptually simple on structured grids, their flexibility is limited for curved or irregular geometries. In contrast, FEM is based on a variational formulation of the PDE and uses piecewise polynomial trial and test functions on a mesh of the domain, which allows geometric features and boundary conditions to be incorporated in a natural and systematic way.

The basic idea of FEM dates back to Courant's use of triangulations and piecewise linear functions in the 1940s [7] and was later developed in structural mechanics, where the term "finite element method" was popularized by Clough and others [6]. Since then, FEM has been placed on a rigorous mathematical foundation using Sobolev spaces and weak formulations of elliptic boundary value problems, leading to abstract convergence and error estimates. These developments are presented in standard monographs such as Ciarlet [5], Brenner–Scott [4], Larson–Bengzon [11], Ern–Guermond [8], and Johnson [10].

## 1.2 Model Problem and Boundary Conditions

As a model problem we consider a prototypical second-order elliptic boundary value problem, namely the two-dimensional Poisson equation with homogeneous Dirichlet boundary conditions. Let  $\Omega \subset \mathbb{R}^2$  be a bounded polygonal domain with boundary  $\partial\Omega$ , and let  $f: \Omega \rightarrow \mathbb{R}$  be a given source term. We seek an unknown function  $u: \Omega \rightarrow \mathbb{R}$  satisfying

$$\begin{aligned} -\Delta u &= f && \text{in } \Omega, \\ u &= 0 && \text{on } \partial\Omega, \end{aligned} \tag{1.1}$$

where  $\Delta$  denotes the Laplace operator. Depending on the physical context,  $u$  may represent the steady-state temperature distribution in a conductor, the electric potential in a dielectric, or a displacement potential in linear elasticity, among others.

Although problem (1.1) is among the simplest second-order elliptic equations, it captures many of the key analytical and numerical features of more general elliptic problems. From an analytical viewpoint, the problem admits a natural weak formulation in the Sobolev space  $H_0^1(\Omega)$ , and the weak solution can be interpreted as the minimizer of an associated energy functional. From a numerical viewpoint, using a conforming finite element space contained in  $H_0^1(\Omega)$  leads to a symmetric positive definite linear system, whose conditioning and approximation properties can be analyzed using standard tools.

To focus on the core structure of the finite element method, we restrict attention to homogeneous Dirichlet boundary conditions  $u = 0$  on  $\partial\Omega$ . This avoids the technical complications arising from nonhomogeneous or mixed boundary conditions, while keeping the Galerkin structure as transparent as possible. Moreover, by choosing  $f$  and  $\Omega$  appropriately, one can construct examples where the exact solution of (1.1) is known analytically, which is particularly useful for validating the numerical implementation. Such manufactured solutions allow us to compute the  $H^1$ - and  $L^2$ -errors explicitly on a sequence of meshes and to study the convergence behavior quantitatively.

### 1.3 Objectives and Organization of the Paper

The aim of this paper is to present, in a reasonably concise yet self-contained manner, the finite element method for the two-dimensional Poisson problem (1.1), and to compare the theoretical a priori error estimates with numerical results obtained from a MATLAB implementation. Our presentation follows the general framework of standard FEM texts such as [5, 11, 8, 10], but emphasizes a step-by-step derivation from basic principles. We use a conforming  $P_1$  finite element space consisting of piecewise linear functions on a triangulation of  $\Omega$ , which is one of the most widely used and simplest finite elements in practice.

We begin by deriving the weak formulation of (1.1) in  $H_0^1(\Omega)$  and by defining the associated bilinear form and linear functional. Next, we introduce a family of triangulations of  $\Omega$  and the corresponding conforming  $P_1$  finite element spaces  $V_{h,0} \subset H_0^1(\Omega)$ . The finite element method is then formulated as a Galerkin approximation: find  $u_h \in V_{h,0}$  such that the weak formulation holds for all test functions  $v_h \in V_{h,0}$ . Under standard assumptions on the domain and the data, both the continuous and discrete problems admit unique solutions, and Céa's lemma allows us to relate the finite element error to the best approximation error in  $V_{h,0}$ .

In order to obtain quantitative convergence results, we employ classical interpolation operators and their approximation properties. Combining these interpolation error estimates with the abstract Galerkin error bound, we derive a priori estimates for the error in the  $H^1$ - and  $L^2$ -norms between the exact solution  $u$  and the finite element solution  $u_h$ . In particular, under the assumption that the exact solution is sufficiently smooth and that the meshes are quasi-uniform, we expect the finite element error to converge with optimal order as the mesh size  $h \rightarrow 0$ .

To verify these theoretical convergence rates in practice, we implement the finite element method in MATLAB and perform numerical experiments. On a sequence of successively refined meshes we compute the finite element solution and evaluate the  $H^1$ - and  $L^2$ -errors. Plotting the errors against the mesh size on a log–log scale and estimating the slopes yields empirical convergence rates, which we compare with the theoretical predictions. The numerical results confirm that the expected optimal rates are indeed observed, thereby supporting the effectiveness and validity of the finite element method for the two-dimensional Poisson equation (1.1).

The paper is organized as follows. In Section 2 we introduce the notation and function spaces used in the variational formulation, and we define the finite element spaces associated with a triangulation of the domain. Section 3 presents the Galerkin finite element method for the Poisson problem (1.1), formulates the continuous and discrete problems, and derives a priori error estimates. Section 4 describes the MATLAB implementation and reports numerical results demonstrating agreement with the theoretical convergence rates. Finally, Section 5 summarizes the main findings and briefly discusses possible extensions to more general elliptic problems, adaptive mesh refinement, and goal-oriented error estimation.

**Code availability.** All MATLAB codes used for the finite element implementation and the numerical experiments in this paper are available in a public GitHub repository: <https://github.com/msb06e7/CDiMath>.

## 2 Preliminaries

In this section we collect the basic notation, function spaces, and finite element spaces that will be used later. The overall approach follows the standard finite element framework presented in, for example, [5, 4, 11, 8, 10]. Throughout this section,  $C$  denotes a positive constant whose value may change from line to line, but which is always independent of the mesh size  $h$ .

### 2.1 Domain, Mesh, and Notation

Let  $\Omega \subset \mathbb{R}^2$  be a bounded polygonal domain with boundary  $\partial\Omega$ . We assume that  $\Omega$  is a Lipschitz domain in the usual sense of Sobolev space theory, so that standard trace and extension theorems hold. [4] The polygonal assumption is convenient for constructing conforming triangulations and is sufficient for the purposes of this paper.

We define the standard inner product on  $L^2(\Omega)$  by

$$(u, v)_{L^2(\Omega)} := \int_{\Omega} u(x) v(x) \, dx \quad (2.1)$$

and the associated norm by

$$\|u\|_{L^2(\Omega)} := (u, u)_{L^2(\Omega)}^{1/2}. \quad (2.2)$$

When the domain is clear from the context, we omit the subscript and simply write  $(u, v)$  and  $\|u\|$ .

We now define a triangulation of the domain  $\Omega$ . Let  $\mathcal{T}_h$  be a finite collection of closed triangles  $K$  such that

- $\overline{\Omega} = \bigcup_{K \in \mathcal{T}_h} K$ ,
- for any two distinct elements  $K, K' \in \mathcal{T}_h$ ,  $\text{int}(K) \cap \text{int}(K') = \emptyset$ ,
- the intersection  $K \cap K'$  of any two elements  $K$  and  $K'$  is either empty, a single vertex, or a single edge.

Such a collection  $\mathcal{T}_h$  is called a *triangulation* of  $\Omega$ . The subscript  $h > 0$  indicates a representative measure of the element size, referred to as the mesh size.

For each element  $K \in \mathcal{T}_h$ , we define its diameter by

$$h_K := \text{diam}(K) = \sup_{x, y \in K} |x - y| \quad (2.3)$$

and the global mesh size  $h$  by

$$h := \max_{K \in \mathcal{T}_h} h_K. \quad (2.4)$$

A family of triangulations  $\{\mathcal{T}_h\}_h$  is said to be *shape-regular* if there exists a constant  $\sigma > 0$  such that for all  $h$  and all  $K \in \mathcal{T}_h$ ,

$$\frac{h_K}{\rho_K} \leq \sigma, \quad (2.5)$$

where  $\rho_K$  denotes the radius of the largest inscribed circle in  $K$  (the inradius). Shape-regularity is a standard assumption in finite element analysis to prevent the appearance of highly degenerate or “sliver” elements.[5, 4]

We denote by

$$\mathcal{N}_h := \{\text{all vertices of } K \in \mathcal{T}_h\} \quad (2.6)$$

the set of all mesh nodes (vertices). The subsets of interior and boundary nodes are defined by

$$\mathcal{N}_h^{\text{int}} := \mathcal{N}_h \cap \Omega, \quad \mathcal{N}_h^{\partial} := \mathcal{N}_h \cap \partial\Omega, \quad (2.7)$$

respectively. These nodes will serve as the degrees of freedom of the finite element space defined in Section 2.3.

## 2.2 Function Spaces

We briefly review the function spaces needed for the variational formulation of the Poisson problem. First, we define

$$L^2(\Omega) := \left\{ u : \Omega \rightarrow \mathbb{R} \mid \int_{\Omega} |u(x)|^2 dx < \infty \right\}. \quad (2.8)$$

For an integer  $m \geq 0$ , the Sobolev space  $H^m(\Omega)$  is given by

$$H^m(\Omega) := \left\{ u \in L^2(\Omega) \mid D^\alpha u \in L^2(\Omega) \text{ for all multi-indices } \alpha \text{ with } |\alpha| \leq m \right\}, \quad (2.9)$$

where  $D^\alpha u$  denotes the weak derivative of  $u$  of order  $\alpha$ .

**Definition of Weak Derivative.** Let  $\Omega \subset \mathbb{R}^d$  be an open set and  $u \in L^1_{\text{loc}}(\Omega)$ . For a multi-index  $\alpha$ , a function  $v \in L^1_{\text{loc}}(\Omega)$  is called the  $\alpha$ -th *weak derivative* of  $u$  if for all test functions  $\varphi \in C_0^\infty(\Omega)$ ,

$$\int_{\Omega} u(x) D^\alpha \varphi(x) dx = (-1)^{|\alpha|} \int_{\Omega} v(x) \varphi(x) dx \quad (2.10)$$

holds. In this case we write  $v = D^\alpha u$  and say that  $u$  admits the weak derivative  $D^\alpha u$ . The weak derivative is unique almost everywhere, and if  $u$  is sufficiently smooth in the classical sense, then the weak derivative coincides with the classical derivative.

In particular,  $H^1(\Omega)$  consists of those functions  $u \in L^2(\Omega)$  whose first-order weak derivatives belong to  $L^2(\Omega)$ . The standard norm on  $H^1(\Omega)$  is

$$\|u\|_{H^1(\Omega)}^2 := \|u\|_{L^2(\Omega)}^2 + \|\nabla u\|_{L^2(\Omega)}^2, \quad (2.11)$$

and the associated seminorm is defined by

$$|u|_{H^1(\Omega)} := \|\nabla u\|_{L^2(\Omega)}. \quad (2.12)$$

We define  $H_0^1(\Omega)$  as the closure of  $C_0^\infty(\Omega)$  in  $H^1(\Omega)$ :

$$H_0^1(\Omega) := \overline{C_0^\infty(\Omega)}^{H^1(\Omega)}. \quad (2.13)$$

Functions in  $H_0^1(\Omega)$  have zero trace on  $\partial\Omega$ , in the sense of Sobolev trace theory, and can thus be viewed as functions that vanish on the boundary. On  $H_0^1(\Omega)$ , the Poincaré inequality implies that the  $H^1$ -norm and the seminorm are equivalent. More precisely, there exists a constant  $C_P > 0$  depending only on  $\Omega$  such that

$$\|u\|_{L^2(\Omega)} \leq C_P \|\nabla u\|_{L^2(\Omega)} \quad \text{for all } u \in H_0^1(\Omega). \quad (2.14)$$

Thus on  $H_0^1(\Omega)$  one may equivalently use

$$\|u\|_{1,\Omega} := \|\nabla u\|_{L^2(\Omega)} \quad (2.15)$$

as a norm, which is equivalent to the full  $H^1$ -norm. For further details on Sobolev spaces and the Poincaré inequality, see [4, 11, 9, 8].

The energy space for the Poisson problem is  $H_0^1(\Omega)$ . The associated energy inner product is defined by

$$(u, v)_e := \int_\Omega \nabla u(x) \cdot \nabla v(x) \, dx, \quad u, v \in H_0^1(\Omega), \quad (2.16)$$

and the corresponding norm is  $\|u\|_e := (u, u)_e^{1/2}$ . By the Poincaré inequality (2.14), this norm is equivalent to the  $H^1$ -norm on  $H_0^1(\Omega)$ .

### 2.3 Finite Element Spaces

We now define the finite element spaces used to discretize the variational formulation of the Poisson problem. We work with conforming piecewise linear (i.e.,  $P_1$ ) finite elements associated with the triangulation  $\mathcal{T}_h$ .

Let  $\hat{K}$  be the reference triangle with vertices  $\hat{a}_1 = (0, 0)$ ,  $\hat{a}_2 = (1, 0)$ , and  $\hat{a}_3 = (0, 1)$ . The space of linear polynomials on  $\hat{K}$  is

$$\mathbb{P}_1(\hat{K}) := \left\{ p : \hat{K} \rightarrow \mathbb{R} \mid p(\hat{x}) = c_1 + c_2 \hat{x}_1 + c_3 \hat{x}_2, \, c_i \in \mathbb{R} \right\}. \quad (2.17)$$

A standard basis of this space is given by the barycentric coordinate functions  $\hat{\lambda}_i$ ,  $i = 1, 2, 3$ , which satisfy

$$\hat{\lambda}_i(\hat{a}_j) = \delta_{ij}, \quad 1 \leq i, j \leq 3. \quad (2.18)$$

For each element  $K \in \mathcal{T}_h$ , we assume there exists an affine bijection  $F_K : \hat{K} \rightarrow K$  of the form

$$F_K(\hat{x}) = B_K \hat{x} + b_K, \quad (2.19)$$

where  $B_K$  is an invertible  $2 \times 2$  matrix and  $b_K \in \mathbb{R}^2$ . This mapping sends the vertices of the reference

triangle to the vertices of  $K$ . The local polynomial space on  $K$  is defined by

$$\mathbb{P}_1(K) := \left\{ p \circ F_K^{-1} \mid p \in \mathbb{P}_1(\hat{K}) \right\}. \quad (2.20)$$

Equivalently, a function  $v : K \rightarrow \mathbb{R}$  belongs to  $\mathbb{P}_1(K)$  if and only if it is the restriction to  $K$  of a linear polynomial defined on all of  $\mathbb{R}^2$ .

The global finite element space corresponding to  $\mathcal{T}_h$  is

$$V_h := \left\{ v_h \in C^0(\bar{\Omega}) \mid v_h|_K \in \mathbb{P}_1(K) \text{ for all } K \in \mathcal{T}_h \right\}. \quad (2.21)$$

To incorporate the Dirichlet boundary condition, we define

$$V_{h,0} := V_h \cap H_0^1(\Omega) = \left\{ v_h \in V_h \mid v_h|_{\partial\Omega} = 0 \right\}. \quad (2.22)$$

The space  $V_{h,0}$  is a finite-dimensional subspace of  $H_0^1(\Omega)$  and will serve as both the trial and test space in the finite element method.

We now describe a convenient basis of  $V_{h,0}$ . For each interior node  $x_i \in \mathcal{N}_h^{\text{int}}$ , we define the global nodal basis function  $\varphi_i \in V_{h,0}$  by

$$\varphi_i(x_j) = \delta_{ij} \quad \text{for all } x_j \in \mathcal{N}_h. \quad (2.23)$$

That is,  $\varphi_i$  is continuous, piecewise linear, and satisfies  $\varphi_i(x_i) = 1$  and  $\varphi_i(x_j) = 0$  for all other nodes  $x_j \in \mathcal{N}_h$ . The collection of basis functions associated with interior nodes forms a basis of  $V_{h,0}$ . If the interior nodes are labeled  $x_1, \dots, x_N$ , then  $\{\varphi_1, \dots, \varphi_N\}$  is a basis of  $V_{h,0}$ , and every  $v_h \in V_{h,0}$  has a unique representation

$$v_h(x) = \sum_{i=1}^N V_i \varphi_i(x) \quad (2.24)$$

for some coefficient vector  $V = (V_1, \dots, V_N)^T \in \mathbb{R}^N$ .

On  $V_{h,0}$  we may use the same inner product and norm as on  $H_0^1(\Omega)$ . When we want to emphasize the discrete structure, we write

$$(u_h, v_h)_e := \int_{\Omega} \nabla u_h(x) \cdot \nabla v_h(x) \, dx, \quad \|u_h\|_e := (u_h, u_h)_e^{1/2}, \quad (2.25)$$

for  $u_h, v_h \in V_{h,0}$ .

## 2.4 Interpolation Operator and Approximation Properties

A central ingredient in the a priori error analysis of the finite element method is the approximation property of the finite element space  $V_{h,0}$ . To quantify how well functions in  $H_0^1(\Omega)$  can be approximated by functions in  $V_{h,0}$ , we introduce a suitable interpolation operator and derive error estimates for it.

The nodal Lagrange interpolation operator  $I_h : C^0(\bar{\Omega}) \rightarrow V_h$  is defined by

$$(I_h u)(x_i) = u(x_i) \quad \text{for all } x_i \in \mathcal{N}_h. \quad (2.26)$$

That is,  $I_h u$  is the unique function in  $V_h$  that agrees with  $u$  at all mesh nodes. If, in addition,  $u$  vanishes on the boundary, then  $u(x_i) = 0$  for all boundary nodes, and hence  $(I_h u)(x_i) = 0$  on  $\mathcal{N}_h^\partial$ , so that  $I_h u \in V_{h,0}$ . For sufficiently smooth  $u \in H_0^1(\Omega)$ , the function  $I_h u$  is a natural candidate for approximating  $u$  in  $V_{h,0}$ .

We now state the standard interpolation error estimates for  $P_1$  finite element spaces on a shape-regular family of triangulations  $\{\mathcal{T}_h\}_h$ . If  $u \in H^2(\Omega) \cap H_0^1(\Omega)$ , then there exists a constant  $C > 0$ , independent of  $u$  and  $h$ , such that

$$\|u - I_h u\|_{H^1(\Omega)} \leq C h \|u\|_{H^2(\Omega)}, \quad (2.27)$$

$$\|u - I_h u\|_{L^2(\Omega)} \leq C h^2 \|u\|_{H^2(\Omega)}. \quad (2.28)$$

In other words, the  $P_1$  finite element space provides first-order accuracy in the  $H^1$ -norm and second-order accuracy in the  $L^2$ -norm for sufficiently smooth functions.

We also record the corresponding local estimates. For each element  $K \in \mathcal{T}_h$ , there exists a constant  $C > 0$ , independent of  $u$  and  $K$ , such that

$$\|u - I_h u\|_{H^1(K)} \leq C h_K \|u\|_{H^2(K)}, \quad (2.29)$$

$$\|u - I_h u\|_{L^2(K)} \leq C h_K^2 \|u\|_{H^2(K)}. \quad (2.30)$$

Summing these local estimates over all elements  $K \in \mathcal{T}_h$  yields the global bounds (2.27) and (2.28).

The above interpolation estimates can be viewed as a special case of the more general Bramble–Hilbert lemma. In the present context, a convenient version of the lemma reads as follows (cf. [4, 5]).

**Theorem 2.1** (A special case of the Bramble–Hilbert lemma). *Let  $\Omega \subset \mathbb{R}^d$  be a bounded domain satisfying appropriate regularity assumptions, and let  $\mathcal{T}_h$  be a shape-regular partition of  $\Omega$ . For an integer  $m \geq 1$  and  $0 \leq k \leq m$ , there exists for each element  $K \in \mathcal{T}_h$  and each  $u \in H^m(K)$  a polynomial  $p \in \mathbb{P}_{m-1}(K)$  such that*

$$\|u - p\|_{H^k(K)} \leq C h_K^{m-k} |u|_{H^m(K)}, \quad 0 \leq k \leq m,$$

where the constant  $C > 0$  depends only on  $m$  and the shape-regularity of the partition, but not on  $u$  or  $h_K$ .

In the case of  $P_1$  finite elements, the interpolation operator  $I_h$  reproduces all linear polynomials on each element, i.e.,  $I_h p = p$  for all  $p \in \mathbb{P}_1(K)$ . Thus, taking  $m = 2$  and  $k = 0, 1$  in the Bramble–Hilbert lemma and choosing  $p = I_h u|_K$ , we obtain the local interpolation error estimates stated above, and hence the global estimates (2.27) and (2.28).

These interpolation error bounds play a key role in the Galerkin error analysis of the next section. In particular, when combined with the abstract Galerkin error estimate (Céa’s lemma), they yield the standard a priori error estimates for the finite element approximation of the Poisson problem.

### 3 Finite Element Method

In this section we derive the weak formulation of the Poisson problem, formulate its finite element approximation using the finite element spaces introduced in Section 2, and present abstract error estimates. We work with the energy space  $V := H_0^1(\Omega)$  and its conforming  $P_1$  finite element subspace  $V_{h,0} \subset V$ . Our discussion follows the standard Hilbert space Galerkin theory as presented, for example, in [5, 4, 11, 8, 10].

#### 3.1 Weak Formulation and Well-posedness

We restate the model problem introduced in Section 1. We consider the Poisson problem

$$\begin{aligned} -\Delta u &= f && \text{in } \Omega, \\ u &= 0 && \text{on } \partial\Omega, \end{aligned} \tag{3.1}$$

where  $\Omega \subset \mathbb{R}^2$  is a bounded polygonal domain and  $f \in L^2(\Omega)$  is a given source term.

To derive the weak formulation, we first assume that  $u$  is sufficiently smooth, say  $u \in C^2(\bar{\Omega})$ , and multiply the equation by a smooth test function  $v \in C_0^\infty(\Omega)$  whose support is contained in  $\Omega$ . Integrating over  $\Omega$  yields

$$\int_\Omega (-\Delta u) v \, dx = \int_\Omega f v \, dx. \tag{3.2}$$

By Green's identity (integration by parts),

$$\int_\Omega (-\Delta u) v \, dx = \int_\Omega \nabla u \cdot \nabla v \, dx - \int_{\partial\Omega} \frac{\partial u}{\partial n} v \, ds, \tag{3.3}$$

where  $\partial u / \partial n$  denotes the normal derivative on the boundary. If we assume in addition that  $v$  vanishes on  $\partial\Omega$ , the boundary term disappears and we obtain

$$\int_\Omega \nabla u \cdot \nabla v \, dx = \int_\Omega f v \, dx. \tag{3.4}$$

We now use the Sobolev spaces defined in Section 2 to formulate this computation rigorously. Let  $V := H_0^1(\Omega)$  and define the bilinear form  $a(\cdot, \cdot)$  and linear functional  $\ell(\cdot)$  by

$$a(u, v) := \int_\Omega \nabla u(x) \cdot \nabla v(x) \, dx, \quad u, v \in V, \tag{3.5}$$

$$\ell(v) := \int_\Omega f(x) v(x) \, dx, \quad v \in V. \tag{3.6}$$

The Poisson problem then admits the following weak formulation.

**Problem 3.1** (Weak formulation). Find  $u \in V$  such that

$$a(u, v) = \ell(v) \quad \text{for all } v \in V. \tag{3.7}$$

If  $f \in L^2(\Omega)$ , it is well known that problem (3.7) admits a unique solution  $u \in V$ . [4, Chapter 5] When

$\Omega$  and  $f$  are sufficiently smooth, this weak solution coincides with the classical solution of (3.1).

The weak formulation can also be viewed as the Euler–Lagrange equation of the energy functional

$$J(v) := \frac{1}{2}a(v, v) - \ell(v) = \frac{1}{2} \int_{\Omega} |\nabla v(x)|^2 dx - \int_{\Omega} f(x) v(x) dx, \quad v \in V. \quad (3.8)$$

Indeed,  $u \in V$  satisfies (3.7) if and only if it is the unique minimizer of  $J$  over  $V$ :

$$J(u) \leq J(v) \quad \text{for all } v \in V. \quad (3.9)$$

This variational perspective is also useful for understanding the Galerkin approximation.

We briefly recall the basic abstract Galerkin theory in a Hilbert space setting. Let  $V$  be a Hilbert space with inner product  $(\cdot, \cdot)_V$  and norm  $\|\cdot\|_V$ , let  $a(\cdot, \cdot): V \times V \rightarrow \mathbb{R}$  be a bilinear form, and let  $\ell(\cdot): V \rightarrow \mathbb{R}$  be a continuous linear functional.

The bilinear form  $a(\cdot, \cdot)$  is said to be *continuous* on  $V$  if there exists a constant  $M > 0$  such that

$$|a(u, v)| \leq M \|u\|_V \|v\|_V \quad (3.10)$$

for all  $u, v \in V$ . It is said to be *coercive* on  $V$  if there exists a constant  $\alpha > 0$  such that

$$a(v, v) \geq \alpha \|v\|_V^2 \quad (3.11)$$

for all  $v \in V$ . Under these assumptions, consider the abstract weak problem

$$\text{Find } u \in V \text{ such that } a(u, v) = \ell(v) \quad \text{for all } v \in V. \quad (3.12)$$

**Theorem 3.1** (Lax–Milgram). *Let  $V$  be a Hilbert space, and let  $a(\cdot, \cdot)$  satisfy the continuity and coercivity conditions (3.10) and (3.11). Suppose that  $\ell$  is a continuous linear functional on  $V$ . Then the weak problem (3.12) admits a unique solution  $u \in V$  and*

$$\|u\|_V \leq \frac{1}{\alpha} \|\ell\|_{V'} \quad (3.13)$$

holds, where  $\alpha$  is the coercivity constant in (3.11) and  $\|\ell\|_{V'}$  denotes the operator norm of  $\ell$  in the dual space  $V'$ .

For the Poisson problem we take  $V = H_0^1(\Omega)$ , equipped with the inner product  $(\cdot, \cdot)_e$  and norm  $\|\cdot\|_e$  defined in Section 2. The bilinear form  $a(\cdot, \cdot)$  satisfies

$$|a(u, v)| = \left| \int_{\Omega} \nabla u \cdot \nabla v dx \right| \leq \|\nabla u\|_{L^2(\Omega)} \|\nabla v\|_{L^2(\Omega)} = \|u\|_e \|v\|_e, \quad (3.14)$$

$$a(v, v) = \int_{\Omega} |\nabla v|^2 dx = \|v\|_e^2, \quad (3.15)$$

so (3.10) and (3.11) hold with  $M = 1$  and  $\alpha = 1$ . Hence, by Theorem 3.1, the weak problem 3.1 has a

unique solution  $u \in V$ .

### 3.2 Galerkin Finite Element Formulation

We now discretize the weak formulation (3.7) using the Galerkin finite element method. With the conforming  $P_1$  finite element space  $V_{h,0} \subset V$  introduced in Section 2, we define the discrete problem by restricting both trial and test functions to  $V_{h,0}$ .

**Problem 3.2** (Galerkin finite element problem). Find  $u_h \in V_{h,0}$  such that

$$a(u_h, v_h) = \ell(v_h) \quad \text{for all } v_h \in V_{h,0}. \quad (3.16)$$

Problem 3.2 is the finite element approximation of the weak problem 3.1. By construction,  $u_h$  can be interpreted as the minimizer of the energy functional  $J$  defined in (3.8), but now restricted to the finite-dimensional subspace  $V_{h,0}$ :

$$u_h = \underset{v_h \in V_{h,0}}{\operatorname{argmin}} J(v_h). \quad (3.17)$$

A fundamental property of the Galerkin approximation is the so-called *Galerkin orthogonality*.

**Proposition 3.2** (Galerkin orthogonality). *Let  $u \in V$  be the solution of the weak problem (3.7) and  $u_h \in V_{h,0}$  the solution of the Galerkin problem (3.16). Then*

$$a(u - u_h, v_h) = 0 \quad \text{for all } v_h \in V_{h,0}. \quad (3.18)$$

*Proof.* For any  $v_h \in V_{h,0}$ , we have by definition

$$a(u, v_h) = \ell(v_h), \quad a(u_h, v_h) = \ell(v_h). \quad (3.19)$$

Subtracting these two equalities yields

$$a(u - u_h, v_h) = 0, \quad (3.20)$$

which is the desired orthogonality relation.  $\square$

### 3.3 Céa's Lemma and Linear System

We now consider a general abstract Galerkin approximation and derive Céa's lemma. Let  $V$  be a Hilbert space, and let  $a(\cdot, \cdot)$  and  $\ell(\cdot)$  satisfy the assumptions of Theorem 3.1. Given a finite-dimensional subspace  $V_h \subset V$  (for the Poisson problem we take  $V_h = V_{h,0}$ ), we define the discrete problem

$$\text{Find } u_h \in V_h \text{ such that } a(u_h, v_h) = \ell(v_h) \quad \text{for all } v_h \in V_h. \quad (3.21)$$

Under the same assumptions, the discrete problem has a unique solution  $u_h \in V_h$ . The Galerkin error  $u - u_h$  satisfies the following basic estimate.

**Theorem 3.3** (Céa's lemma). *Let  $V$  be a Hilbert space, and assume that  $a(\cdot, \cdot)$  and  $\ell(\cdot)$  satisfy the assumptions of Theorem 3.1. Let  $u \in V$  be the solution of (3.12), and  $u_h \in V_h$  the solution of (3.21). Then*

$$\|u - u_h\|_V \leq \frac{M}{\alpha} \inf_{v_h \in V_h} \|u - v_h\|_V, \quad (3.22)$$

where  $M$  and  $\alpha$  are the continuity and coercivity constants in (3.10) and (3.11), respectively.

*Proof.* The abstract version of Galerkin orthogonality states that

$$a(u - u_h, v_h) = 0 \quad \text{for all } v_h \in V_h. \quad (3.23)$$

Let  $w_h \in V_h$  be arbitrary. By coercivity,

$$\alpha \|u - u_h\|_V^2 \leq a(u - u_h, u - u_h). \quad (3.24)$$

Adding and subtracting  $w_h$  in the second argument, we obtain

$$a(u - u_h, u - u_h) = a(u - u_h, u - w_h) + a(u - u_h, w_h - u_h). \quad (3.25)$$

The second term vanishes by (3.23), since  $w_h - u_h \in V_h$ . Hence

$$a(u - u_h, u - u_h) = a(u - u_h, u - w_h). \quad (3.26)$$

By continuity and the Cauchy–Schwarz inequality,

$$|a(u - u_h, u - w_h)| \leq M \|u - u_h\|_V \|u - w_h\|_V. \quad (3.27)$$

Combining the above inequalities, we obtain

$$\alpha \|u - u_h\|_V^2 \leq M \|u - u_h\|_V \|u - w_h\|_V. \quad (3.28)$$

If  $u \neq u_h$ , we can divide by  $\|u - u_h\|_V$  to obtain

$$\|u - u_h\|_V \leq \frac{M}{\alpha} \|u - w_h\|_V. \quad (3.29)$$

Since  $w_h \in V_h$  was arbitrary, taking the infimum over  $V_h$  yields (3.22). In the trivial case  $u = u_h$  the estimate is obvious.  $\square$

For the Poisson problem, with  $V = H_0^1(\Omega)$  and  $\|\cdot\|_V = \|\cdot\|_e$ , we have  $M = \alpha = 1$ , and hence for the finite element solution  $u_h \in V_{h,0}$ ,

$$\|u - u_h\|_e \leq \inf_{v_h \in V_{h,0}} \|u - v_h\|_e. \quad (3.30)$$

Thus the Galerkin finite element solution  $u_h$  is as good as the best approximation to  $u$  from  $V_{h,0}$  in the energy norm.

To compute the  $P_1$  finite element approximation in practice, we must derive the linear algebraic system corresponding to the Galerkin problem (3.16). As in Section 2, let  $x_1, \dots, x_N$  denote the interior nodes, and let  $\{\varphi_1, \dots, \varphi_N\}$  be the associated global nodal basis functions in  $V_{h,0}$ . Any  $u_h \in V_{h,0}$  can be written uniquely as

$$u_h(x) = \sum_{j=1}^N U_j \varphi_j(x) \quad (3.31)$$

for a coefficient vector  $U = (U_1, \dots, U_N)^T \in \mathbb{R}^N$ .

Inserting this expansion into (3.16) and choosing  $v_h = \varphi_i$  for  $i = 1, \dots, N$ , we obtain

$$a \left( \sum_{j=1}^N U_j \varphi_j, \varphi_i \right) = \ell(\varphi_i), \quad i = 1, \dots, N. \quad (3.32)$$

Using the linearity of  $a(\cdot, \cdot)$  in the first argument, we have

$$\sum_{j=1}^N U_j a(\varphi_j, \varphi_i) = \ell(\varphi_i), \quad i = 1, \dots, N. \quad (3.33)$$

Defining the stiffness matrix  $A \in \mathbb{R}^{N \times N}$  and the load vector  $b \in \mathbb{R}^N$  by

$$A_{ij} := a(\varphi_j, \varphi_i) = \int_{\Omega} \nabla \varphi_j(x) \cdot \nabla \varphi_i(x) dx, \quad b_i := \ell(\varphi_i) = \int_{\Omega} f(x) \varphi_i(x) dx, \quad (3.34)$$

we arrive at the linear system

$$AU = b. \quad (3.35)$$

Since the bilinear form  $a(\cdot, \cdot)$  is symmetric, the matrix  $A$  is symmetric. Coercivity of  $a(\cdot, \cdot)$  on  $V_{h,0}$  implies that  $A$  is positive definite. In practice, the entries of  $A$  and  $b$  are computed by assembling contributions from each element  $K \in \mathcal{T}_h$ , using local basis functions to compute local stiffness matrices and load vectors, which are then added to the global matrix and vector. More details on finite element matrices and solvers can be found in [11, 3]. The corresponding MATLAB implementation is available in the GitHub repository cited in the Code availability paragraph.

### 3.4 A Priori Error Estimates

We now combine the abstract Galerkin error estimate (3.30) with the interpolation error bounds from Section 2 to derive a priori error estimates for the finite element approximation of the Poisson problem.

### Error estimate in the $H^1$ -norm

We first derive an a priori error estimate in the  $H^1$ -norm. Recall that the interpolation operator  $I_h: C^0(\bar{\Omega}) \rightarrow V_h$  is defined by

$$(I_h u)(x_i) = u(x_i) \quad \text{for all } x_i \in \mathcal{N}_h. \quad (3.36)$$

If  $u \in H_0^1(\Omega)$  is sufficiently smooth, then  $I_h u \in V_{h,0}$ .

**Theorem 3.4** (A priori error estimate in the  $H^1$ -norm). *Let  $u \in H^2(\Omega) \cap H_0^1(\Omega)$  be the solution of the Poisson problem (3.7), and let  $u_h \in V_{h,0}$  be the solution of the finite element problem (3.16). Then there exists a constant  $C > 0$ , independent of  $u$  and  $h$ , such that*

$$\|u - u_h\|_{H^1(\Omega)} \leq C h \|u\|_{H^2(\Omega)}. \quad (3.37)$$

*Proof.* By Céa's lemma (3.30),

$$\|u - u_h\|_{H^1(\Omega)} \leq \inf_{v_h \in V_{h,0}} \|u - v_h\|_{H^1(\Omega)}. \quad (3.38)$$

Choosing  $v_h = I_h u$  and using the interpolation estimate (2.27), we obtain

$$\|u - u_h\|_{H^1(\Omega)} \leq \|u - I_h u\|_{H^1(\Omega)} \leq C h \|u\|_{H^2(\Omega)}, \quad (3.39)$$

which proves (3.37).  $\square$

The above estimate holds under the regularity assumption  $u \in H^2(\Omega)$ , which can be justified by elliptic regularity theory. For the Poisson equation we have, for example, the following result.

**Theorem 3.5** (Elliptic regularity). *Let  $\Omega \subset \mathbb{R}^2$  be a bounded domain satisfying suitable regularity assumptions. In particular, assume that  $\Omega$  is a convex polygonal domain and that  $f \in L^2(\Omega)$ . Then the solution  $u \in H_0^1(\Omega)$  of the Poisson problem (3.7) satisfies*

$$u \in H^2(\Omega) \cap H_0^1(\Omega), \quad \|u\|_{H^2(\Omega)} \leq C \|f\|_{L^2(\Omega)} \quad (3.40)$$

for some constant  $C > 0$  independent of  $f$ .

The above regularity property is classical for convex polygonal domains; see, for instance, Evans [9] and McLean [12]. Thus, under the elliptic regularity assumption, the  $P_1$  finite element method achieves first-order convergence in the  $H^1$ -norm.

### Error estimate in the $L^2$ -norm

We now derive a sharper error estimate in the  $L^2$ -norm using the Aubin–Nitsche duality argument. Let  $e := u - u_h$  denote the error. Consider the following dual (or adjoint) problem: find  $z \in V$  such that

$$a(v, z) = (e, v)_{L^2(\Omega)} \quad \text{for all } v \in V. \quad (3.41)$$

By Theorem 3.1, this problem has a unique solution  $z \in V$ . Under additional regularity assumptions on  $\Omega$  and  $e$ , we may assume that  $z \in H^2(\Omega) \cap H_0^1(\Omega)$ .

**Theorem 3.6** (A priori error estimate in the  $L^2$ -norm). *Suppose that the assumptions of Theorem 3.4 hold and that the solution  $z$  of the dual problem (3.41) satisfies*

$$\|z\|_{H^2(\Omega)} \leq C \|e\|_{L^2(\Omega)} \quad (3.42)$$

for some constant  $C > 0$ . Then there exists a constant  $C > 0$ , independent of  $u$  and  $h$ , such that

$$\|u - u_h\|_{L^2(\Omega)} \leq C h^2 \|u\|_{H^2(\Omega)}. \quad (3.43)$$

*Proof.* Testing the dual problem (3.41) with  $v = e$  yields

$$\|e\|_{L^2(\Omega)}^2 = (e, e)_{L^2(\Omega)} = a(e, z). \quad (3.44)$$

Using Galerkin orthogonality and the interpolant  $I_h z \in V_{h,0}$ , we obtain

$$a(e, z) = a(e, z - I_h z), \quad (3.45)$$

and hence

$$\|e\|_{L^2(\Omega)}^2 = a(e, z - I_h z). \quad (3.46)$$

Using continuity and the Cauchy–Schwarz inequality,

$$|a(e, z - I_h z)| \leq \|\nabla e\|_{L^2(\Omega)} \|\nabla(z - I_h z)\|_{L^2(\Omega)} = \|e\|_{H^1(\Omega)} \|z - I_h z\|_{H^1(\Omega)}. \quad (3.47)$$

Applying the interpolation estimate (2.27) to  $z$ , we have

$$\|z - I_h z\|_{H^1(\Omega)} \leq C h \|z\|_{H^2(\Omega)}. \quad (3.48)$$

Combining (3.46)–(3.48), we obtain

$$\|e\|_{L^2(\Omega)}^2 \leq C h \|e\|_{H^1(\Omega)} \|z\|_{H^2(\Omega)}. \quad (3.49)$$

Using the regularity assumption (3.42), we further obtain

$$\|e\|_{L^2(\Omega)}^2 \leq C h \|e\|_{H^1(\Omega)} \|e\|_{L^2(\Omega)}. \quad (3.50)$$

If  $\|e\|_{L^2(\Omega)} \neq 0$ , we divide both sides by  $\|e\|_{L^2(\Omega)}$  to obtain

$$\|e\|_{L^2(\Omega)} \leq C h \|e\|_{H^1(\Omega)}. \quad (3.51)$$

Finally, applying the  $H^1$ -error estimate (3.37), we deduce

$$\|e\|_{L^2(\Omega)} \leq C h \|u - u_h\|_{H^1(\Omega)} \leq C h^2 \|u\|_{H^2(\Omega)}, \quad (3.52)$$

which is (3.43).  $\square$

The assumption (3.42) is a form of elliptic regularity for the dual problem. For example, if  $\Omega$  is a convex polygonal domain and  $f \in L^2(\Omega)$ , then both the original and dual problems enjoy the  $H^2$ -regularity property stated above. In this setting, the  $P_1$  finite element method achieves second-order convergence in the  $L^2$ -norm.

In summary, for the Poisson problem (3.1), the Galerkin finite element method is well-defined, and under the assumption that the exact solution  $u$  is sufficiently smooth, the finite element solution  $u_h$  satisfies the standard a priori error estimates

$$\|u - u_h\|_{H^1(\Omega)} \leq C h \|u\|_{H^2(\Omega)}, \quad (3.53)$$

$$\|u - u_h\|_{L^2(\Omega)} \leq C h^2 \|u\|_{H^2(\Omega)}. \quad (3.54)$$

In Section 4 we examine how these theoretical convergence rates manifest themselves in numerical experiments based on a MATLAB implementation.

## 4 Numerical Experiments

In this section we verify the convergence results of Section 3 by means of numerical experiments. We consider test problems with known exact solutions and approximate them using the conforming  $P_1$  finite element spaces  $V_{h,0}$  defined in Section 2. For a sequence of successively refined meshes we compute the errors in the  $H^1$ - and  $L^2$ -norms and compare the observed convergence rates with the a priori error estimates of Theorems 3.4 and 3.6.

Throughout this section we consider the Poisson problem

$$-\Delta u = f \quad \text{in } \Omega, \quad u = 0 \quad \text{on } \partial\Omega,$$

introduced in Section 1. The weak solution  $u \in H_0^1(\Omega)$  and the Galerkin finite element solution  $u_h \in V_{h,0}$

are defined as in Section 3. We employ the manufactured solution approach: we first choose a sufficiently smooth exact solution  $u$  and then define  $f = -\Delta u$  to construct the corresponding test problem.

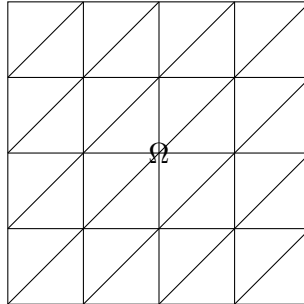


Figure 1: Example of a uniform triangulation of the unit square  $\Omega = (0, 1)^2$ . Each rectangle is split along a diagonal to form the standard triangular mesh used for  $P_1$  finite elements.

As illustrated in Figure 1, we employ a uniform triangulation of the unit square: we first partition the square into rectangles and then split each rectangle along a diagonal to obtain a triangular mesh.

#### 4.1 Test Problems

We now describe the specific test problems used in the numerical experiments. For convenience, all examples are defined on the unit square

$$\Omega := (0, 1) \times (0, 1),$$

with homogeneous Dirichlet boundary conditions  $u = 0$  on  $\partial\Omega$ . In each case the exact solution is chosen to be smooth on  $\bar{\Omega}$  so that the regularity assumptions of Theorems 3.4 and 3.6 are satisfied.

##### Test Problem 1: Smooth solution on the unit square

As a first example we consider a problem with a smooth solution vanishing on the boundary. We define

$$u(x, y) := \sin(\pi x) \sin(\pi y), \quad (x, y) \in \bar{\Omega}. \quad (4.1)$$

A straightforward computation shows that

$$\frac{\partial^2 u}{\partial x^2}(x, y) = -\pi^2 \sin(\pi x) \sin(\pi y), \quad \frac{\partial^2 u}{\partial y^2}(x, y) = -\pi^2 \sin(\pi x) \sin(\pi y),$$

so that

$$\Delta u(x, y) = -2\pi^2 \sin(\pi x) \sin(\pi y),$$

and hence

$$f(x, y) := -\Delta u(x, y) = 2\pi^2 \sin(\pi x) \sin(\pi y). \quad (4.2)$$

Since  $\sin(\pi x)$  and  $\sin(\pi y)$  vanish when  $x = 0, 1$  or  $y = 0, 1$ , we have  $u = 0$  on  $\partial\Omega$ . Thus, the pair  $(u, f)$  given by (4.1) and (4.2) defines an exact solution–data pair for the Poisson problem.

The solution  $u$  is infinitely differentiable on  $\overline{\Omega}$ , hence belongs to  $H^2(\Omega)$  (indeed, to  $H^k(\Omega)$  for all  $k$ ), and the dual problem also enjoys sufficient regularity. Therefore, according to the theory in Section 3, we expect first-order convergence in the  $H^1$ -norm and second-order convergence in the  $L^2$ -norm.

### Test Problem 2: Polynomial solution

As a second example we consider a problem with a polynomial solution. We define

$$u(x, y) := x^2(1-x)^2y^2(1-y)^2, \quad (x, y) \in \overline{\Omega}. \quad (4.3)$$

Since  $x(1-x)$  and  $y(1-y)$  vanish when  $x = 0, 1$  or  $y = 0, 1$ , we again have  $u = 0$  on  $\partial\Omega$ . Defining

$$f(x, y) := -\Delta u(x, y), \quad (4.4)$$

we obtain an exact solution of the Poisson problem with data  $f$ .

Here too, the function  $u$  is a polynomial on  $\overline{\Omega}$ , hence lies in  $H^2(\Omega)$ , and the dual problem is sufficiently regular. Therefore, as in Test Problem 1, we expect first-order convergence in the  $H^1$ -norm and second-order convergence in the  $L^2$ -norm.

In the numerical experiments we use one or both of the above test problems. For each test problem we compute finite element solutions on a sequence of refined meshes, evaluate the  $H^1$ - and  $L^2$ -errors, and compare the observed convergence rates with the theoretical predictions.

## 4.2 MATLAB Implementation

We describe the main steps of the MATLAB implementation used in the numerical experiments. The overall structure is that of a standard finite element algorithm: mesh generation, assembly of the stiffness matrix and load vector, imposition of boundary conditions, solution of the linear system, and error computation. The relevant MATLAB codes are available in the public GitHub repository mentioned in the Code availability paragraph.

### Mesh generation

For each refinement level  $k = 0, 1, 2, \dots$ , we generate a uniform triangulation of the unit square  $\Omega = (0, 1)^2$ . We first divide  $\Omega$  into an  $N_0 \times N_0$  grid of rectangles and then split each rectangle along a prescribed diagonal to obtain the initial mesh. At subsequent refinement levels we halve the grid spacing in each coordinate direction.

If  $h_k$  denotes the mesh size at refinement level  $k$ , then

$$h_0 = \frac{1}{N_0}$$

with, for example,  $N_0 = 4$ , and

$$h_k := 2^{-k} h_0, \quad k = 0, 1, 2, \dots$$

We denote the triangulation at level  $k$  by  $\mathcal{T}_{h_k}$  and the corresponding finite element space by  $V_{h_k,0}$ .

### Assembly of the stiffness matrix and load vector

For a given triangulation  $\mathcal{T}_h$ , we assemble the stiffness matrix  $A$  and load vector  $b$  defined by (3.34). The assembly is performed elementwise.

For each triangle  $K \in \mathcal{T}_h$ , we consider the local nodal basis functions  $\{\varphi_{K,1}, \varphi_{K,2}, \varphi_{K,3}\}$  associated with the three vertices of  $K$ . The local stiffness matrix  $A^{(K)} \in \mathbb{R}^{3 \times 3}$  and local load vector  $b^{(K)} \in \mathbb{R}^3$  are defined by

$$A_{mn}^{(K)} := \int_K \nabla \varphi_{K,n}(x) \cdot \nabla \varphi_{K,m}(x) \, dx, \quad b_m^{(K)} := \int_K f(x) \varphi_{K,m}(x) \, dx,$$

for  $m, n = 1, 2, 3$ . These local contributions are then assembled into the global matrix  $A$  and vector  $b$  via the element-to-global degree of freedom mapping.

The above integrals are approximated by numerical quadrature (e.g. triangular Gauss integration). For  $P_1$  elements and smooth right-hand side  $f$ , a second-order accurate three-point Gauss–Legendre quadrature rule on triangles suffices to obtain the theoretical convergence rates.

### Application of boundary conditions

The homogeneous Dirichlet boundary condition  $u = 0$  on  $\partial\Omega$  is incorporated when forming the linear system  $AU = b$ .

In our approach,  $V_{h,0}$  is defined to consist of functions that vanish at boundary nodes, so degrees of freedom are associated only with interior nodes  $x_i \in \mathcal{N}_h^{\text{int}}$ . Basis functions corresponding to boundary nodes are not included in  $V_{h,0}$ , so we effectively construct from the outset a reduced system involving only interior degrees of freedom.

An alternative implementation would assemble a system including both interior and boundary nodes and then enforce  $U_i = 0$  at boundary nodes by modifying the corresponding rows and columns. In the present work, however, we directly work with  $V_{h,0}$  and include only interior degrees of freedom in the system.

### Solution of the linear system

At each refinement level  $k$  we solve the symmetric positive definite linear system

$$A^{(k)} U^{(k)} = b^{(k)},$$

where  $A^{(k)}$  and  $b^{(k)}$  are the stiffness matrix and load vector associated with  $V_{h_k,0}$ , and  $U^{(k)}$  is the vector of unknown coefficients.

For the mesh sizes considered here, the system size is moderate, and we can use MATLAB's backslash operator to solve the system by a direct method:

$$U^{(k)} = A^{(k)} \backslash b^{(k)}.$$

Once the coefficient vector  $U^{(k)}$  is computed, the finite element solution  $u_{h_k}$  can be evaluated as

$$u_{h_k}(x) = \sum_{j=1}^{N_k} U_j^{(k)} \varphi_j^{(k)}(x),$$

where  $\{\varphi_1^{(k)}, \dots, \varphi_{N_k}^{(k)}\}$  is the nodal basis of  $V_{h_k,0}$  and  $N_k$  is the number of interior nodes at level  $k$ .

### 4.3 Error Measurement and Convergence Study

We next describe how the errors of the finite element solutions are computed and how convergence rates are estimated from a sequence of meshes.

#### Discrete norms and error computation

Given the exact solution  $u$  and the finite element solution  $u_h$ , we define the error by

$$e_h := u - u_h.$$

**$L^2$ -error.** The error in the  $L^2$ -norm is given by

$$\|e_h\|_{L^2(\Omega)} = \left( \int_{\Omega} |u(x) - u_h(x)|^2 dx \right)^{1/2}.$$

In the implementation, this integral is approximated by a quadrature rule applied elementwise:

$$\|e_h\|_{L^2(\Omega)}^2 \approx \sum_{K \in \mathcal{T}_h} \sum_{q=1}^{N_q} w_q^{(K)} |u(x_q^{(K)}) - u_h(x_q^{(K)})|^2,$$

where  $\{x_q^{(K)}, w_q^{(K)}\}_{q=1}^{N_q}$  are the quadrature points and weights on element  $K$ .

**$H^1$ -error.** The error in the  $H^1$ -norm is

$$\|e_h\|_{H^1(\Omega)}^2 = \|e_h\|_{L^2(\Omega)}^2 + \|\nabla e_h\|_{L^2(\Omega)}^2,$$

where

$$\|\nabla e_h\|_{L^2(\Omega)}^2 = \int_{\Omega} |\nabla u(x) - \nabla u_h(x)|^2 dx.$$

Again, we approximate this integral by quadrature:

$$\|\nabla e_h\|_{L^2(\Omega)}^2 \approx \sum_{K \in \mathcal{T}_h} \sum_{q=1}^{N_q} w_q^{(K)} |\nabla u(x_q^{(K)}) - \nabla u_h(x_q^{(K)})|^2.$$

Since  $u_h$  is piecewise linear, its gradient is constant on each element  $K$ . Thus, for each element we need to compute  $\nabla u_h$  only once, which simplifies the implementation.

### Convergence rates

To study the convergence behavior of the method, we consider a sequence of meshes with mesh sizes  $h_0 > h_1 > \dots > h_K$  (e.g.  $h_k = h_{k-1}/2$ ). Let

$$E_{H^1}^{(k)} := \|u - u_{h_k}\|_{H^1(\Omega)}, \quad E_{L^2}^{(k)} := \|u - u_{h_k}\|_{L^2(\Omega)}$$

denote the errors at level  $k$ .

Assuming that the errors behave like

$$E_{H^1}^{(k)} \approx C_1 h_k^{p_1}, \quad E_{L^2}^{(k)} \approx C_2 h_k^{p_2},$$

for some constants  $C_1, C_2 > 0$  and rates  $p_1, p_2 > 0$ , we can estimate the observed convergence rates using consecutive refinement levels:

$$p_1^{(k)} := \frac{\log(E_{H^1}^{(k-1)}/E_{H^1}^{(k)})}{\log(h_{k-1}/h_k)}, \quad k = 1, 2, \dots, \quad (4.5)$$

$$p_2^{(k)} := \frac{\log(E_{L^2}^{(k-1)}/E_{L^2}^{(k)})}{\log(h_{k-1}/h_k)}, \quad k = 1, 2, \dots. \quad (4.6)$$

In the case of uniform refinement with  $h_k = h_{k-1}/2$  these expressions simplify to

$$p_1^{(k)} = \log_2 \left( \frac{E_{H^1}^{(k-1)}}{E_{H^1}^{(k)}} \right), \quad p_2^{(k)} = \log_2 \left( \frac{E_{L^2}^{(k-1)}}{E_{L^2}^{(k)}} \right).$$

According to the a priori estimates of Section 3 (Theorems 3.4 and 3.6), for sufficiently fine meshes we should observe

$$p_1^{(k)} \approx 1, \quad p_2^{(k)} \approx 2.$$

In practice, we present tables summarizing the errors  $E_{H^1}^{(k)}$ ,  $E_{L^2}^{(k)}$  and the corresponding estimated rates  $p_1^{(k)}$ ,  $p_2^{(k)}$  for each refinement level, and we visualize the relation between the errors and the mesh size on log–log plots. These numerical results show that the finite element method reproduces the theoretically predicted convergence behavior for the two-dimensional Poisson problem.

## 4.4 Experimental Results

The a priori error estimates obtained in Section 3 predict that, under sufficient smoothness and elliptic regularity, the  $P_1$  finite element method satisfies

$$\|u - u_h\|_{H^1(\Omega)} = O(h), \quad \|u - u_h\|_{L^2(\Omega)} = O(h^2),$$

which are the *optimal* convergence rates in view of the approximation order of  $P_1$  elements. In this subsection we verify numerically that these rates are indeed realized in computations.

Using the implementation described above, we compute the errors for Test Problem 1 and Test Problem 2 on refinement levels  $k = 1, \dots, 5$ . For each level we record the mesh size  $h$ , the errors  $E_{H^1}^{(k)}$  and  $E_{L^2}^{(k)}$ , and the estimated convergence rates  $p_1^{(k)}$  and  $p_2^{(k)}$  defined in (4.5) and (4.6). Here  $N$  denotes the number of subintervals in each coordinate direction, and the mesh size is  $h = 1/N$ .

Table 1: Mesh size, errors, and observed convergence rates for Test Problem 1.

$k$	$N$	$h$	$\ e\ _{H^1(\Omega)}$	$p_1^{(k)}$	$\ e\ _{L^2(\Omega)}$	$p_2^{(k)}$
1	4	$2.50 \times 10^{-1}$	$8.431 \times 10^{-1}$	—	$7.596 \times 10^{-2}$	—
2	8	$1.25 \times 10^{-1}$	$4.324 \times 10^{-1}$	0.963	$2.041 \times 10^{-2}$	1.896
3	16	$6.25 \times 10^{-2}$	$2.176 \times 10^{-1}$	0.991	$5.201 \times 10^{-3}$	1.972
4	32	$3.13 \times 10^{-2}$	$1.090 \times 10^{-1}$	0.998	$1.307 \times 10^{-3}$	1.993
5	64	$1.56 \times 10^{-2}$	$5.452 \times 10^{-2}$	0.999	$3.270 \times 10^{-4}$	1.998

Table 2: Mesh size, errors, and observed convergence rates for Test Problem 2.

$k$	$N$	$h$	$\ e\ _{H^1(\Omega)}$	$p_1^{(k)}$	$\ e\ _{L^2(\Omega)}$	$p_2^{(k)}$
1	4	$2.50 \times 10^{-1}$	$3.838 \times 10^{-3}$	—	$3.176 \times 10^{-4}$	—
2	8	$1.25 \times 10^{-1}$	$2.181 \times 10^{-3}$	0.815	$9.815 \times 10^{-5}$	1.694
3	16	$6.25 \times 10^{-2}$	$1.127 \times 10^{-3}$	0.952	$2.602 \times 10^{-5}$	1.916
4	32	$3.13 \times 10^{-2}$	$5.683 \times 10^{-4}$	0.988	$6.604 \times 10^{-6}$	1.978
5	64	$1.56 \times 10^{-2}$	$2.848 \times 10^{-4}$	0.997	$1.657 \times 10^{-6}$	1.994

We also show log–log plots of the  $H^1$ - and  $L^2$ -errors versus the mesh size  $h$  for both test problems in Figures 2 and 3. In each figure we include reference lines of slope 1 and 2, corresponding to  $O(h)$  and  $O(h^2)$ , to facilitate comparison with the observed convergence behavior.

From Tables 1 and 2 we observe that, for sufficiently fine meshes, the estimated convergence rates  $p_1^{(k)}$  approach 1 and  $p_2^{(k)}$  approach 2 in both test problems. This shows that the theoretical a priori error estimates of Theorems 3.4 and 3.6 are not only upper bounds but are *saturated* in the sense that the finite element method attains the optimal convergence rates allowed by the approximation order of  $P_1$  elements.

In other words, for the test problems considered here, which satisfy the elliptic regularity assumptions with  $u \in H^2(\Omega)$ , the  $H^1$ -error converges at first order and the  $L^2$ -error at second order, in accordance

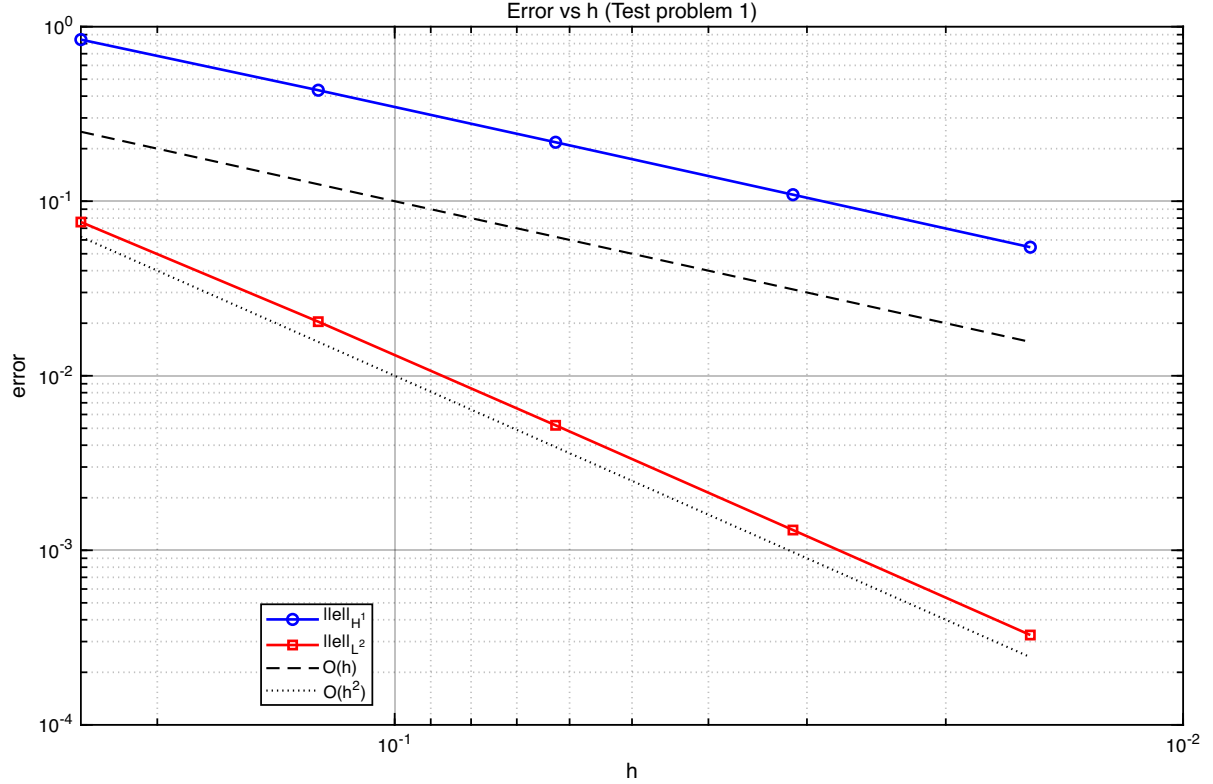


Figure 2: Log–log plot of the  $H^1$ - and  $L^2$ -errors versus mesh size  $h$  for Test Problem 1. The dashed lines indicate the reference rates  $O(h)$  and  $O(h^2)$  predicted by theory.

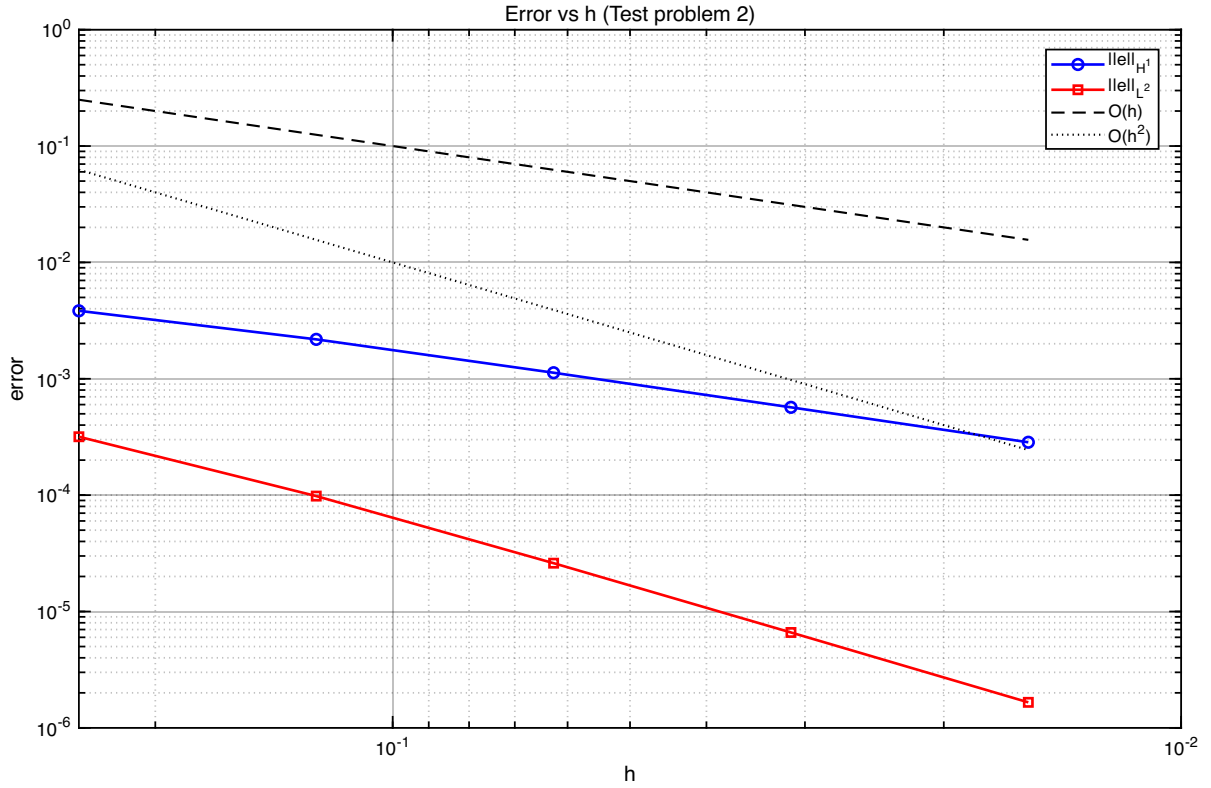


Figure 3: Log–log plot of the  $H^1$ - and  $L^2$ -errors versus mesh size  $h$  for Test Problem 2. The dashed lines indicate the theoretical optimal convergence rates  $O(h)$  and  $O(h^2)$  for  $P_1$  finite elements.

with the theoretical predictions. These numerical results confirm that the finite element implementation considered in this paper exhibits *convergence-optimal* behavior for the two-dimensional Poisson equation.

## 5 Application: Potential Flow Past a Simplified Ground Vehicle

In this section we apply the finite element method to a two-dimensional potential flow model around a simplified ground vehicle. The geometry is designed to mimic the cross-sectional shape of a Cybertruck-like car, represented as a polygonal body suspended slightly above a flat ground plane. The goal is not to perform a quantitatively accurate aerodynamic design study, but rather to illustrate how the abstract FEM framework from the previous sections can be used to set up and analyze a physically meaningful Laplace-type boundary value problem on a geometrically nontrivial domain.[2, 1]

### 5.1 Geometric model

We consider a two-dimensional channel domain consisting of a large outer rectangular box, a flat ground block covering the entire bottom part of the box, and a polygonal vehicle cross-section above the ground. Let  $\Omega_{\text{box}}$  denote the outer rectangle,  $\Omega_g$  the rectangular ground region, and  $\Omega_c$  the polygonal car body. The fluid domain is then given by

$$\Omega := \Omega_{\text{box}} \setminus (\overline{\Omega_g} \cup \overline{\Omega_c}).$$

The boundary of  $\Omega$  is decomposed as

$$\partial\Omega = \Gamma_{\text{in}} \cup \Gamma_{\text{out}} \cup \Gamma_{\text{wall}},$$

where  $\Gamma_{\text{in}}$  is the inflow boundary on the left side of the channel,  $\Gamma_{\text{out}}$  is the outflow boundary on the right side, and  $\Gamma_{\text{wall}}$  consists of the union of the top wall, the ground surface, and the car surface.

The car body is modeled as a convex polygon with five vertices. The lower two vertices define a slightly inclined base segment, the upper two vertices define the front and rear corners of the roof, and the remaining vertex is the roof peak. The polygon is positioned such that there is a narrow underbody gap between the car base and the ground, reflecting the importance of the flow between the chassis and the road surface for vehicle aerodynamics. The entire configuration is uniformly scaled to obtain a sufficiently large computational domain, while keeping the relative proportions of the car and ground unchanged. The triangulation of  $\Omega$  is shown in Figure 4.

### 5.2 Potential flow model and boundary conditions

We describe the flow by a scalar velocity potential  $\Phi : \Omega \rightarrow \mathbb{R}$ , and define the velocity field by

$$\mathbf{u} = -\nabla\Phi.$$

Here  $\mathbf{u}$  denotes the fluid velocity vector, which we distinguish from the scalar Poisson solution  $u$  used in Sections 1–4. We assume the flow is steady, incompressible, inviscid, and irrotational in the bulk of the domain. Under these assumptions the velocity potential satisfies the Laplace equation

$$-\Delta\Phi = 0 \quad \text{in } \Omega. \quad (5.1)$$

The boundary conditions are chosen to model a uniform flow entering from the left, exiting at the right, and sliding tangentially along the walls and the car surface:

$$\frac{\partial\Phi}{\partial n} = 1 \quad \text{on } \Gamma_{\text{in}}, \quad (5.2)$$

$$\Phi \approx 0 \quad \text{on } \Gamma_{\text{out}}, \quad (5.3)$$

$$\frac{\partial\Phi}{\partial n} = 0 \quad \text{on } \Gamma_{\text{wall}}. \quad (5.4)$$

Here  $n$  denotes the outward unit normal vector. On  $\Gamma_{\text{in}}$  the Neumann condition (5.2) imposes approximately constant normal velocity into the domain, so that the free-stream velocity is of order one in non-dimensional units. The condition (5.3) prescribes an effective reference level for the potential at the outlet. In our implementation this is enforced weakly via a Robin penalization of the form

$$\frac{\partial\Phi}{\partial n} + \kappa(\Phi - 0) = 0 \quad \text{on } \Gamma_{\text{out}},$$

with a large penalty parameter  $\kappa \gg 1$ , so that  $\Phi \approx 0$  on  $\Gamma_{\text{out}}$  in the discrete solution. Finally, on  $\Gamma_{\text{wall}}$  we impose the homogeneous Neumann condition (5.4), which corresponds to impermeable slip boundaries: the normal component of the velocity vanishes, but tangential slip is allowed.

We also introduce a non-dimensional Bernoulli-type pressure indicator

$$p_B := \frac{1}{2}(1 - |\mathbf{u}|^2), \quad (5.5)$$

which can be interpreted as a normalized static pressure under the assumption of unit density and unit free-stream speed, in analogy with the Bernoulli relation used in classical aerodynamics [1]. Regions of large  $|\mathbf{u}|$  correspond to locally reduced  $p_B$  and thus low pressure.

### 5.3 Finite element formulation

Let  $V := H^1(\Omega)$  and define the bilinear form  $a : V \times V \rightarrow \mathbb{R}$  and the linear functional  $\ell : V \rightarrow \mathbb{R}$  by

$$\begin{aligned} a(u, v) &= \int_{\Omega} \nabla u \cdot \nabla v \, dx + \int_{\Gamma_{\text{out}}} \kappa u v \, ds, \\ \ell(v) &= \int_{\Gamma_{\text{in}}} g_N v \, ds + \int_{\Gamma_{\text{out}}} \kappa g_D v \, ds, \end{aligned}$$

where  $g_N = 1$  on  $\Gamma_{\text{in}}$  and  $g_D = 0$  on  $\Gamma_{\text{out}}$ , and  $\kappa$  is the penalty parameter used in the Robin condition. The weak formulation of (5.1)–(5.4) then reads:

*Find  $\Phi \in V$  such that*

$$a(\Phi, v) = \ell(v) \quad \text{for all } v \in V. \quad (5.6)$$

Let  $\mathcal{T}_h$  be a conforming triangulation of  $\Omega$  and let  $V_h \subset V$  be the standard  $P_1$  finite element space of continuous, piecewise affine functions on  $\mathcal{T}_h$ . The discrete problem is:

*Find  $\Phi_h \in V_h$  such that*

$$a(\Phi_h, v_h) = \ell(v_h) \quad \text{for all } v_h \in V_h. \quad (5.7)$$

In matrix form, (5.7) becomes

$$(A + R)\Phi = \mathbf{r},$$

where  $A$  is the stiffness matrix associated with the interior term  $\int_{\Omega} \nabla u_h \cdot \nabla v_h \, dx$ ,  $R$  is the boundary contribution arising from the Robin term on  $\Gamma_{\text{out}}$ , and  $\mathbf{r}$  collects the Neumann and Robin data. Once the nodal coefficients  $\Phi$  are computed, the discrete velocity field is obtained elementwise by

$$\mathbf{u}_h = -\nabla \Phi_h,$$

and the pressure indicator  $p_B$  is evaluated according to (5.5).

## 5.4 MATLAB implementation

The finite element method described above is implemented in MATLAB using custom routines for geometry construction, mesh generation, matrix assembly, and postprocessing.

**Geometry and mesh.** The polygonal geometry is defined in the function `CarGeom.m`, which returns the decomposed geometry data `gd`, `ns`, and `sf` in the format expected by `decsg`. The outer box, ground block, and car polygon are combined via a constructive solid geometry formula of the form

$$\mathbf{sf} = 'R1-G1-C1',$$

so that the fluid domain is the difference of the outer box and the solid subdomains. The initial mesh is generated by

$$[p, e, t] = \text{initmesh}(g, 'hmax', h_{\text{max}}),$$

with  $h_{\text{max}}$  chosen proportional to the domain size, and can be further refined using `refinemesh` if necessary. An example of the resulting mesh is shown in Figure 4.

**Assembly and solution.** The stiffness matrix  $A$  is assembled by a routine `StiffnessAssembler2D` that loops over all triangles  $K \in \mathcal{T}_h$ , computes the gradients of the local hat functions, and accumulates the contributions  $a|_K(\varphi_i, \varphi_j)$  into a global sparse matrix. The Robin and Neumann boundary terms are

assembled by a routine `RobinAssembler2D` that iterates over all boundary edges, evaluates the midpoint geometry, and integrates the one-dimensional edge mass matrix. The large penalty parameter  $\kappa$  is applied only on the outflow part of the boundary, while the inflow Neumann flux is imposed on the left boundary. The final linear system is solved by MATLAB's backslash operator:

$$\Phi = (A + R) \backslash \mathbf{r}.$$

**Postprocessing.** The elementwise gradient of  $\Phi_h$  is computed by the built-in function `pdegrad`, from which the velocity components  $(u_{1,h}, u_{2,h})$  and speed  $|\mathbf{u}_h|$  are obtained. The pressure indicator  $p_B$  is then evaluated at the element centroids. Several diagnostic plots are produced:

- the triangulation of  $\Omega$  (Figure 4),
- equipotential lines of  $\Phi_h$  (Figure 5),
- the velocity field, visualized by arrows or streamlines (Figure 6),
- the normalized Bernoulli pressure  $p_B$  (Figure 7).

All figures are exported with a white background and black axis and label colors to facilitate direct inclusion in the final report.

## 5.5 Numerical results and discussion of potential flow

Figure 5 shows the equipotential lines of the discrete velocity potential  $\Phi_h$ . Near the inflow boundary the contours are almost straight and vertical, corresponding to an almost uniform left-to-right flow. As the streamlines approach the car, the equipotential lines bend around the polygonal body and the ground, indicating acceleration of the flow above the roof and through the underbody gap, and deceleration in front of the vehicle. In the far downstream region the potential gradually relaxes toward the homogeneous state prescribed at the outflow.

The corresponding velocity field is plotted in Figure 6. Above the roof, the streamlines are compressed and the velocity magnitude is significantly larger than the free-stream value, which implies a local decrease of the Bernoulli pressure  $p_B$  in this region. Along the front face of the car the flow is deflected upward and downward, creating a stagnation zone with small velocity and relatively high pressure. The underbody gap between the car and the ground channels the flow into a narrow passage; the velocity in this gap is higher than in the free stream, leading to a low-pressure region that contributes to the vertical force on the vehicle (a simple manifestation of ground effect in this potential model).

Figure 7 displays the normalized Bernoulli pressure field  $p_B$  defined in (5.5). High-pressure regions are observed near the front stagnation area and immediately behind the car base, while the roof and underbody regions exhibit significantly reduced pressure due to flow acceleration. In a more realistic viscous flow these features would be modified by boundary layers and flow separation, which are not captured by

the potential flow approximation. Nevertheless, the present model already reveals qualitatively correct trends in the pressure distribution around a blunt ground vehicle.

From a numerical point of view, the discrete solution is stable and smooth, and the mesh resolution in the underbody gap is sufficiently fine to resolve the main flow features. Refining the mesh further leads to only minor changes in the velocity and pressure fields, indicating that the finite element approximation has reached an asymptotic regime for this problem. This example demonstrates that the abstract Galerkin framework developed earlier can be applied in a straightforward manner to nontrivial geometries and boundary conditions relevant to engineering applications, and that relatively simple MATLAB implementations are sufficient to obtain informative potential flow visualizations around a simplified ground vehicle.

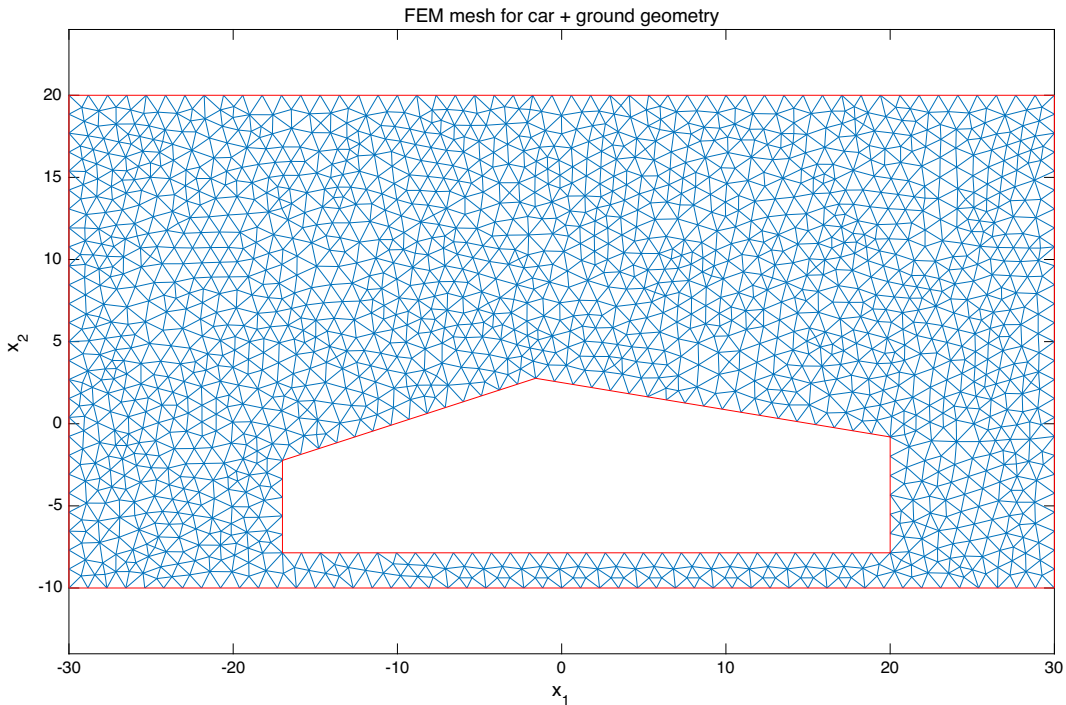


Figure 4: Triangular mesh of the computational domain around the simplified car body and ground.

## 6 Conclusion

In this paper we have studied the conforming  $P_1$  finite element method for the two-dimensional Poisson equation

$$-\Delta u = f \quad \text{in } \Omega, \quad u = 0 \quad \text{on } \partial\Omega$$

from both theoretical and numerical perspectives. We first formulated the weak problem in the Sobolev space  $H_0^1(\Omega)$ , with bilinear form  $a(u, v) = \int_{\Omega} \nabla u \cdot \nabla v \, dx$  and linear functional  $\ell(v) = \int_{\Omega} fv \, dx$ . Using the Lax–Milgram theorem, we established existence and uniqueness of the weak solution and interpreted it as the minimizer of the associated energy functional. On this basis we introduced the Galerkin finite element method on the conforming  $P_1$  subspace  $V_{h,0} \subset H_0^1(\Omega)$ , derived Galerkin orthogonality and Céa’s

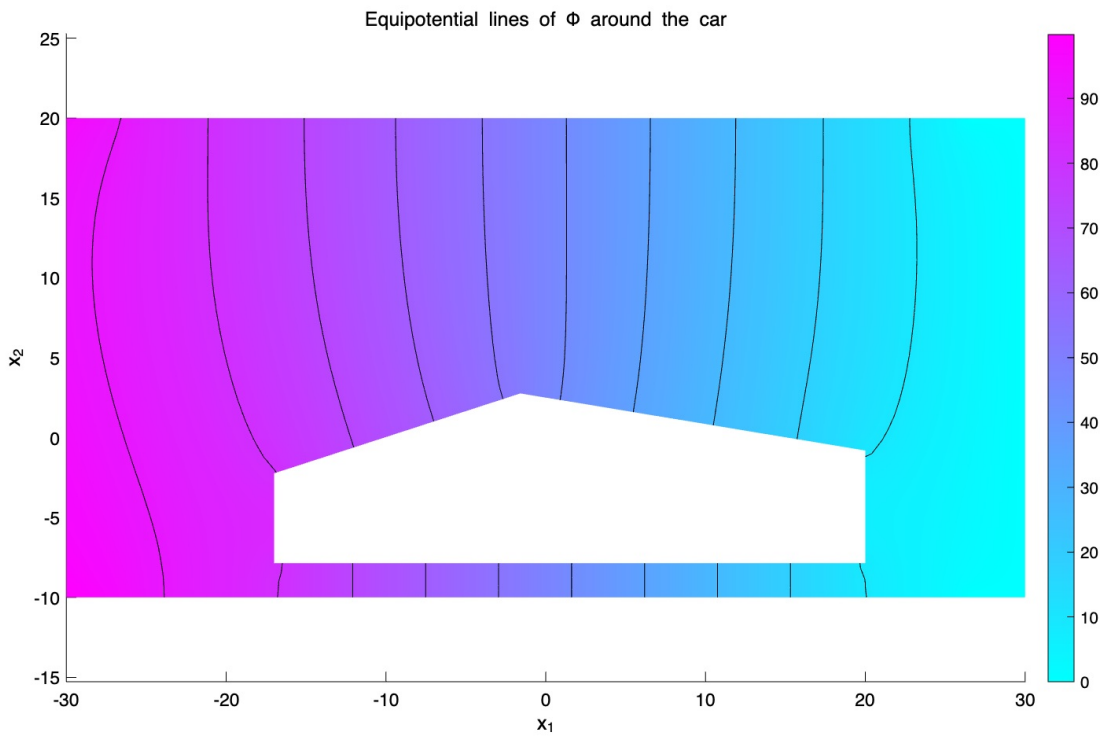


Figure 5: Equipotential lines of the discrete velocity potential  $\Phi_h$  for the car potential flow problem.

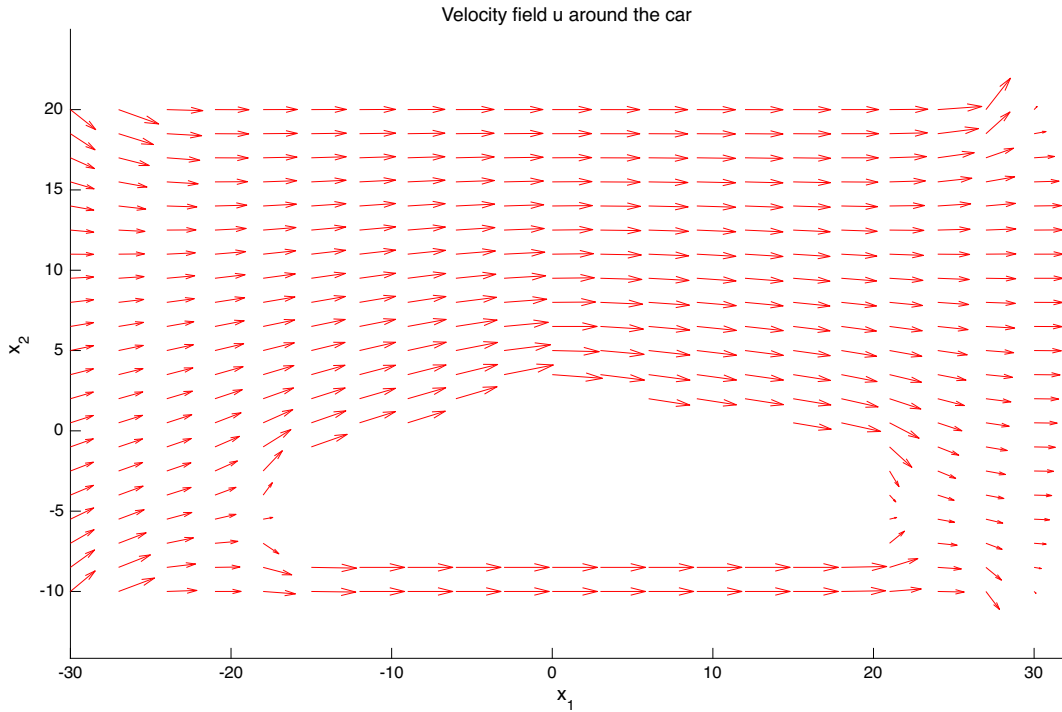


Figure 6: Finite element approximation of the velocity field  $\mathbf{u}_h = -\nabla\Phi_h$  around the car body.

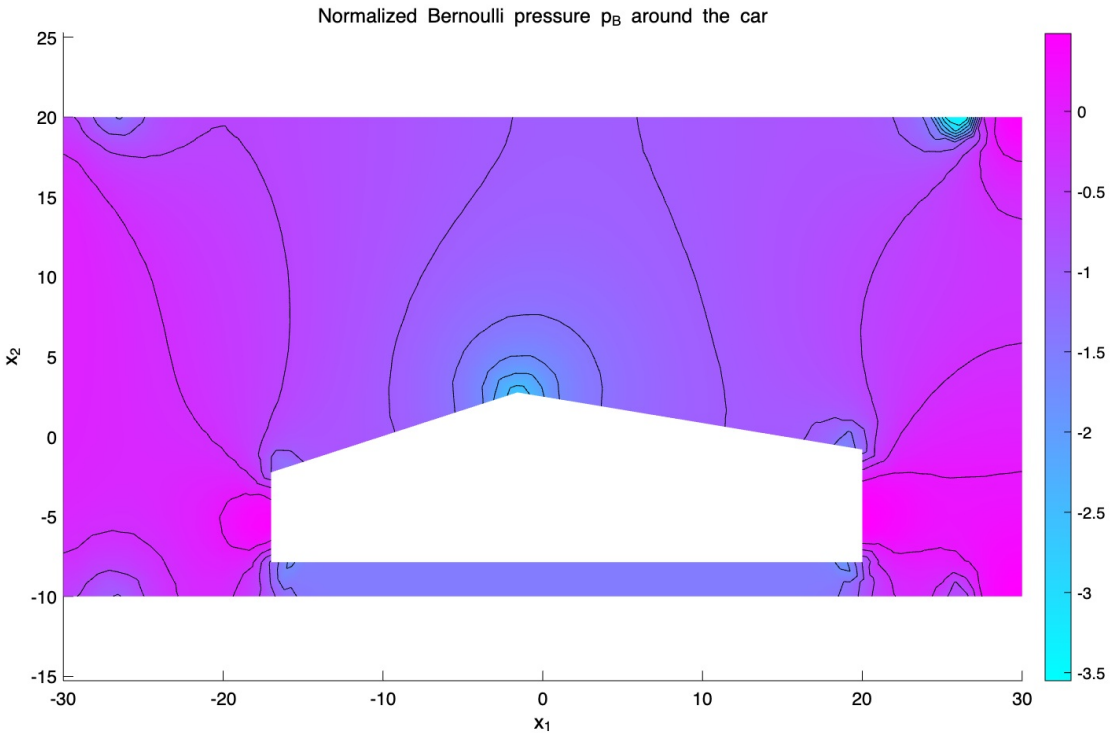


Figure 7: Normalized Bernoulli pressure  $p_B = \frac{1}{2}(1 - |\mathbf{u}_h|^2)$  around the simplified car body.

lemma, and combined them with interpolation error estimates to obtain the standard a priori bounds: first-order convergence in the  $H^1$ -norm and second-order convergence in the  $L^2$ -norm under the usual elliptic regularity assumptions.

To verify these theoretical results, we carried out numerical experiments on the unit square  $\Omega = (0, 1)^2$  using manufactured solutions, as described in Section 4. For a sequence of uniformly refined triangular meshes we assembled the stiffness matrix and load vector for the  $P_1$  finite element method, solved the resulting linear systems, and computed the  $H^1$ - and  $L^2$ -errors using exact expressions for the solution and its gradient. The observed convergence rates, obtained from error tables and log-log plots, are very close to the predicted rates of order  $O(h)$  in  $H^1$  and  $O(h^2)$  in  $L^2$ . This confirms that the implemented method attains the optimal convergence behavior allowed by the approximation order of piecewise linear finite elements for the two-dimensional Poisson problem.

In Section 5 we then applied the same finite element framework to a more involved model problem: potential flow past a simplified ground vehicle. The flow was described by a velocity potential satisfying the Laplace equation on a channel-type domain obtained by subtracting a polygonal car body and a ground block from a large rectangle. By imposing a Neumann inflow condition, a Robin-type outflow condition, and slip (homogeneous Neumann) conditions on the car surface and walls, we obtained a Laplace-type boundary value problem that fits naturally into the variational setting developed earlier. Using the same  $P_1$  finite element machinery and a MATLAB implementation based on `CarGeom.m`, we computed the potential, reconstructed the velocity field, and evaluated a normalized Bernoulli pressure

indicator. The resulting equipotential lines, velocity plots, and pressure contours illustrate physically reasonable features such as flow acceleration over the roof, underbody channeling between the car and the ground, and corresponding low- and high-pressure regions. This example demonstrates that the abstract Galerkin framework and the basic  $P_1$  implementation can be transferred almost verbatim from a simple diffusion model to a geometrically nontrivial potential flow problem with mixed boundary conditions.

The present work has several limitations. Both the theoretical analysis and the quantitative convergence study focus on a scalar Poisson model with homogeneous Dirichlet boundary conditions and smooth data on regular domains, and we restrict ourselves to the lowest-order conforming  $P_1$  elements on uniformly refined meshes. The potential flow example, while geometrically more realistic, still relies on an inviscid, irrotational approximation and does not capture viscous boundary layers or flow separation.

There are several natural directions for future work. One possibility is to extend the analysis and implementation to more general elliptic problems with variable coefficients, mixed or nonhomogeneous boundary conditions, and nonsmooth data. Another is to incorporate residual-based a posteriori error estimators and adaptive mesh refinement strategies, which would be particularly useful for resolving localized features such as boundary layers near the car surface or strong gradients in the underbody region. It would also be interesting to investigate higher-order finite elements and anisotropic meshes for improved accuracy at comparable computational cost. Finally, replacing the potential flow model by more realistic viscous or time-dependent flow models, such as the steady or unsteady Navier–Stokes equations, would provide a natural next step toward using the finite element method as a practical tool for aerodynamic analysis and design.

## References

- [1] J. D. Anderson. *Fundamentals of Aerodynamics*. McGraw-Hill, New York, 5 edition, 2011.
- [2] G. K. Batchelor. *An Introduction to Fluid Dynamics*. Cambridge University Press, Cambridge, 1967.
- [3] D. Braess. *Finite Elements: Theory, Fast Solvers, and Applications in Solid Mechanics*. Cambridge University Press, Cambridge, 3 edition, 2007.
- [4] S. C. Brenner and L. R. Scott. *The Mathematical Theory of Finite Element Methods*. Springer, New York, 3 edition, 2008.
- [5] P. G. Ciarlet. *The Finite Element Method for Elliptic Problems*. Society for Industrial and Applied Mathematics, Philadelphia, 2002.
- [6] R. W. Clough. The finite element method in plane stress analysis. In *Proceedings of the 2nd ASCE Conference on Electronic Computation*, pages 345–378, 1960.
- [7] R. Courant. Variational methods for the solution of problems of equilibrium and vibrations. *Bulletin of the American Mathematical Society*, 49:1–23, 1943.

- [8] A. Ern and J.-L. Guermond. *Theory and Practice of Finite Elements*, volume 159 of *Applied Mathematical Sciences*. Springer, New York, 2004.
- [9] L. C. Evans. *Partial Differential Equations*, volume 19 of *Graduate Studies in Mathematics*. American Mathematical Society, Providence, RI, 2 edition, 2010.
- [10] C. Johnson. *Numerical Solution of Partial Differential Equations by the Finite Element Method*. Cambridge University Press, Cambridge, 1987.
- [11] M. G. Larson and F. Bengzon. *The Finite Element Method: Theory, Implementation, and Applications*. Springer, Berlin, 2013.
- [12] W. McLean. *Strongly Elliptic Systems and Boundary Integral Equations*. Cambridge University Press, Cambridge, 2000.